Predicting the Dynamic Crushing Response of a Composite Honeycomb Energy Absorber Using Solid-Element-Based Models in LS-DYNA®

Karen E. Jackson
NASA Langley Research Center
Hampton, VA

Abstract

This paper describes an analytical study that was performed as part of the development of an externally deployable energy absorber (DEA) concept. The concept consists of a composite honeycomb structure that can be stowed until needed to provide energy attenuation during a crash event, much like an external airbag system. One goal of the DEA development project was to generate a robust and reliable Finite Element Model (FEM) of the DEA that could be used to accurately predict its crush response under dynamic loading. The results of dynamic crush tests of 50-, 104-, and 68-cell DEA components are presented, and compared with simulation results from a solid-element FEM. Simulations of the FEM were performed in LS-DYNA®* to compare the capabilities of three different material models: MAT 63 (crushable foam), MAT 26 (honeycomb), and MAT 126 (modified honeycomb). These material models are evaluated to determine if they can be used to accurately predict both the uniform crushing and final compaction phases of the DEA for normal and off-axis loading conditions.

Introduction

Since its inception in 2006, the NASA Subsonic Rotary Wing (SRW) Aeronautics Program in Rotorcraft Crashworthiness has focused attention on two areas of research: the development of an externally deployable energy absorbing (DEA) concept, and improved prediction of rotorcraft crashworthiness [1]. The DEA concept is a composite honeycomb structure that can be deployed, much like an external airbag system, to provide energy attenuation [2-4]. Both external airbags [5, 6] and the DEA are viable concepts to improve the crash performance of the legacy fleet without requiring major vehicle overhaul. DEA deployment is achieved through a unique and patented flexible hinge at each junction of the cell walls. This feature allows the energy absorber to be stowed in a packed configuration and then readily deployed either radially (multidirectional energy absorption) or linearly (unidirectional energy absorption), as depicted in Figure 1. Like conventional honeycomb, once expanded, the DEA is transformed into an efficient orthotropic cellular structure, with greater strength and stiffness along the cell axis as compared to the transverse directions.

A building block approach was utilized in developing the DEA concept that involved materials testing of its constituent material (Kevlar™-129 fabric with Reinfusion™ 8601 epoxy resin); three-point-bend tests of single hexagonal cells; dynamic compression tests of multi-cell DEA components; multi-terrain vertical drop tests of a composite fuselage section retrofitted with DEA blocks; and, a full-scale crash test of an MD-500 helicopter retrofitted with the DEA.

---

*The use of trademarks or names of manufacturers in this report is for accurate reporting and does not constitute an official endorsement, either expressed or implied, of such products or manufacturers by the National Aeronautics and Space Administration.

Findings from the experimental development program are described in References 3, 4, and 7. At each phase of development, finite element simulations using the nonlinear, explicit transient dynamic code LS-DYNA® [8, 9] accompanied experimental testing. Results from these simulation studies are documented in References 3-4, 10-15.

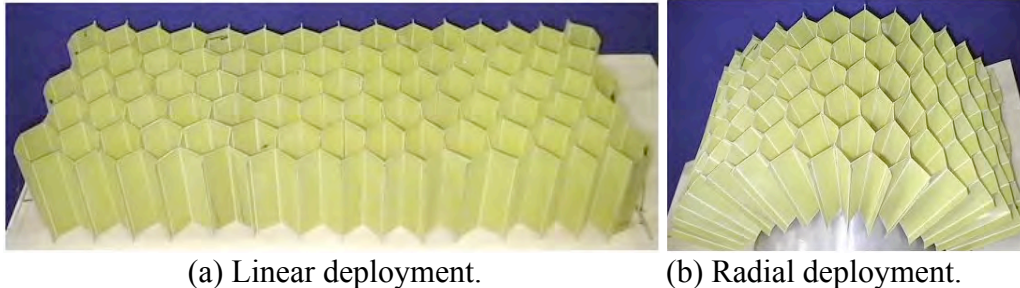(a) Linear deployment.   (b) Radial deployment.

Figure 1. Photographs showing deployment methods of the DEA.

This paper will focus on the results of a simulation study in which solid-element-based models were created to predict the dynamic crushing response of DEA multi-cell components. Three different material definitions available in LS-DYNA® were assigned to the solid elements, including MAT 63 (crushable foam), MAT 26 (honeycomb), and MAT 126 (modified honeycomb). These material models are evaluated to determine if they can accurately predict both the uniform crushing and compaction phases of the DEA for normal and off-axis loading conditions.

DEA Multi-Cell Component Crush Testing

Three multi-cell DEA components were manufactured using a hexagonal cell geometry in which the cell wall edge length was 1.0-in. and the nominal cell wall thickness was 0.01-in. Each of these components was fabricated of a single layer of Kevlar™-129 fabric/epoxy oriented at ±45° with respect to the longitudinal cell axis. Based on the fabrication process, two of the six cell walls within each hexagonal cell consisted of two layers of fabric glued together, and thus had double thickness. Two of the DEA components, consisting of 50 and 104 cells, were manufactured such that the longitudinal axes of the cells were oriented vertically, or in the same direction as loading. These components were designed to provide an average crush stress of approximately 20-psi [3]. A third DEA component, composed of 68 cells, was fabricated such that the longitudinal axis of each cell was canted by 27° with respect to the loading direction. The top surface of each DEA component was curved slightly to reduce the high peak loads that can otherwise occur during initial impact. Also, transverse holes were drilled into the DEA to allow entrapped air to escape. Information on the method used to fabricate the DEA components is found in Reference 3.

Dynamic crush tests were performed by raising a rigid block with known mass to a given height above the test article, and then releasing it to impact a deployed DEA. The DEA was held in place on the ground using double-sided tape. The rigid block was constrained to slide along vertical rods using low friction bearings. A single accelerometer was mounted to the rigid block to record the vertical acceleration response during impact. The dimensions of each DEA, and the impact mass and velocity conditions for each test are listed in Table 1.

Table 1. Details of DEA Component Crush Testing

Number of Cells	Cell Orientation*	Length, in.	Width, in.	Height, in.	Weight of impact block, lb.	Velocity at impact, in/s
50	0°	16	12.4	6.0	412.5	195.6
104	0°	21	15.8	10.0	477.2	266.4
68	27°	16	14.0	6.7	477.2	183.6

*with respect to the vertical, or loading, direction

50-Cell DEA Crush Test
The smallest of the three DEA components, consisting of 50 cells, was impacted with a rigid mass weighing 412.5-lb at a velocity of 195.6-in/s. Pre- and post-test photographs of the 50-cell component are shown in Figures 2(a) and (b), respectively. The measured acceleration time history is plotted in Figure 3(a), and the integrated velocity and displacement time histories are plotted in Figures 3(b) and (c), respectively. An average acceleration of approximately 7.1-g was determined for the time interval of 0.0-0.03 seconds (s), prior to the large increase in acceleration due to compaction of the DEA. At 0.042-s, a maximum acceleration of 64-g was achieved, after which time unloading of the DEA occurred. Also, the maximum vertical deformation of the DEA was 5.6-inches. Given that the original height of the DEA was 6-in, a crush stroke of 93% is obtained.
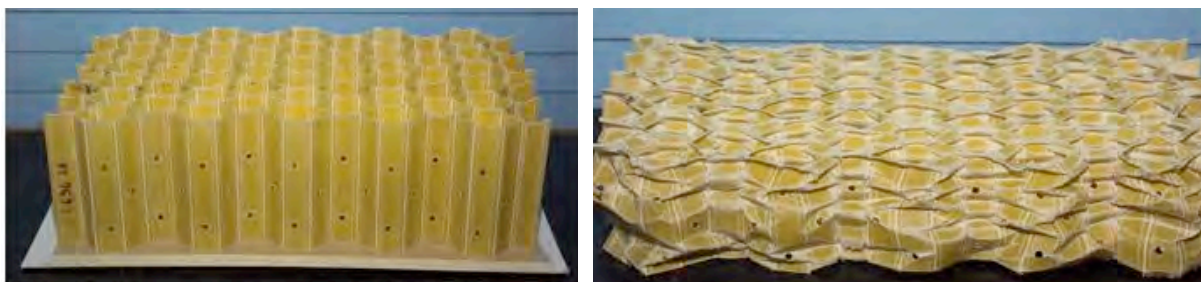
(a) Pre-test photograph.   (b) Post-test photograph.

Figure 2. Pre- and post-test photographs of the deployed 50-cell DEA component.
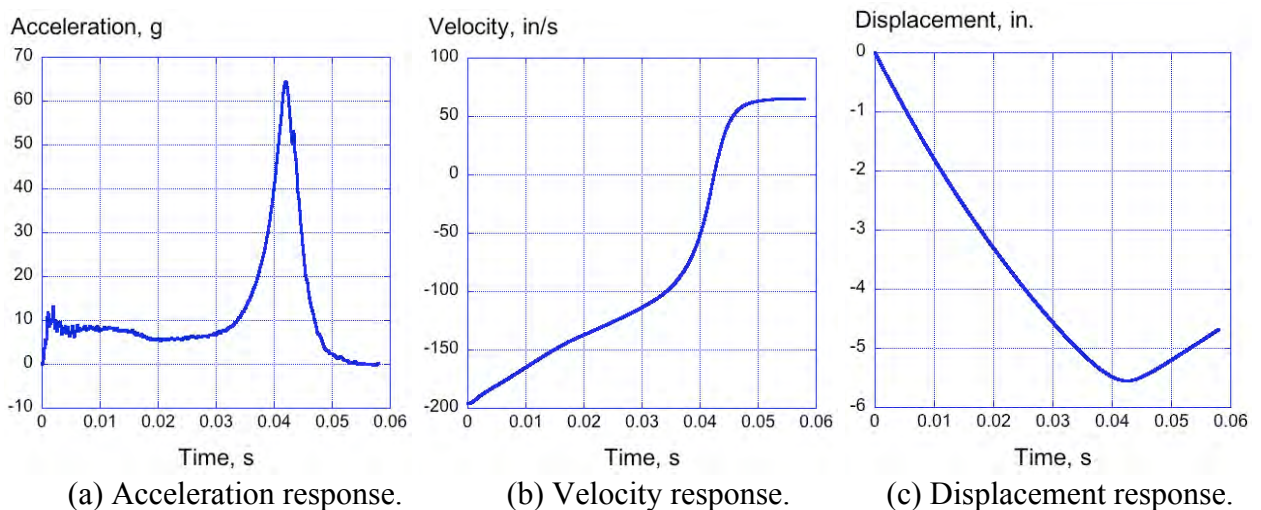
(a) Acceleration response.   (b) Velocity response.   (c) Displacement response.

Figure 3. Time-history results for the 50-cell DEA component.

A close-up photograph of the post-test specimen is shown in Figure 4 to highlight the primary deformation and failure modes of the DEA. The DEA dissipates kinetic energy through cell wall folding and plastic hinge formation. In addition, some delamination and tearing at the cell wall junctions were observed.

104-Cell DEA Crush Test
The largest DEA component was impacted at 266.4-in/s by a 477.2-lb rigid block. As with the 50-cell component, the cells in the 104-cell DEA component were oriented in the vertical, or loading, direction. The measured acceleration time history is plotted in Figure 5(a), and the integrated velocity and displacement time histories are plotted in Figures 5(b) and (c), respectively.
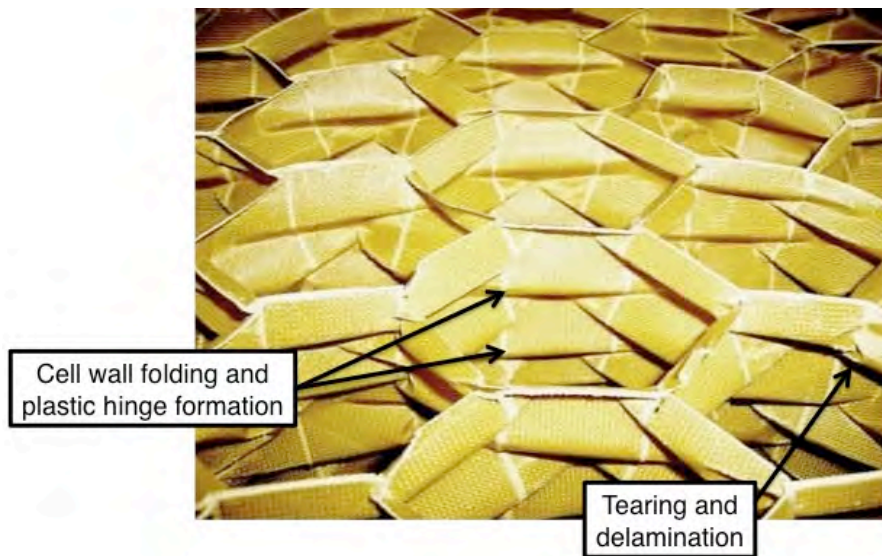

Figure 4. Photograph illustrating the deformation and failure modes exhibited by the DEA.

(a) Acceleration response.   (b) Velocity response.   (c) Displacement response.
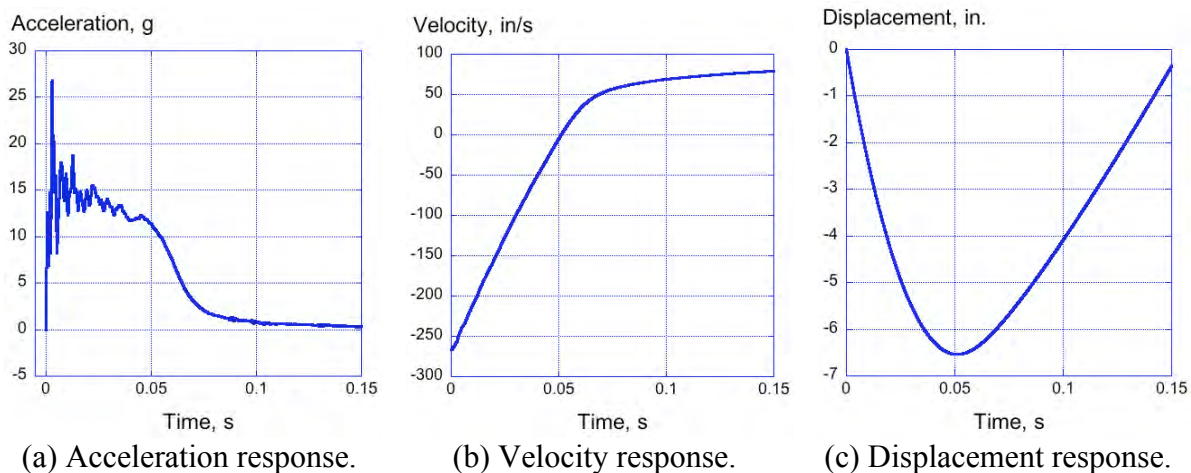
Figure 5. Time-history results for the 104-cell DEA component.

An average acceleration of 14.3-g was determined for the time interval of 0.0-0.03 seconds. For a maximum displacement of 6.6-in., a crush stroke of 65.6% was obtained for the 104-cell DEA. It is interesting to note the differences in acceleration responses between the 50- and the 104-cell

DEA components, shown in Figures 3(a) and 5(a), respectively. The acceleration response of the 50-cell DEA indicates that the component reached compaction, causing a large increase in acceleration near the end of the pulse. However, the acceleration response of the 104-cell DEA indicates that the specimen did not reach the compaction phase, even though a higher impact mass and velocity were used during the impact test. The difference is attributed to the greater cross-sectional area and height of the 104-cell DEA compared with the 50-cell component.

68-Cell DEA Crush Test
A 68-cell DEA was fabricated such that the longitudinal axis of the hexagonal cells was canted by 27° with respect to the vertical direction. This component was fabricated and tested specifically to determine how the DEA would respond under off-axis loading. The bottom surface of the DEA was potted to a flat plate prior to the impact test. The test was conducted by dropping a 477.2-lb block onto the DEA at a vertical velocity of 183.6-in/s.

Acceleration, velocity, and displacement time histories are shown in Figures 6(a), (b), and (c), respectively. The acceleration curve achieves an initial acceleration of 10-g at 0.004-s, subsequently drops to 5-g and then begins to increase to a second peak of 28-g, which occurs at 0.0475-s. The initial reduction in acceleration following the 10-g peak is attributed to global buckling or collapse of the cells in the curved upper region and on the perimeter of the DEA. The second peak of 28-g is due to compaction of the DEA component. Given a maximum displacement of 5.6-in., a crush stoke of 83.6% was determined. An average acceleration of 6.5-g was calculated for the time interval 0.0-0.03 seconds. This value is only 8.5% lower than the value obtained for the 50-cell DEA component, which had all of its cells oriented in the same direction as the loading axis. The crush response of the 68-cell DEA was recorded using high-speed video and several photos taken from the video are shown in Figure 7. These photos indicate that the crushing response of the DEA is fairly uniform, despite the higher shear loading present in the off-axis test.

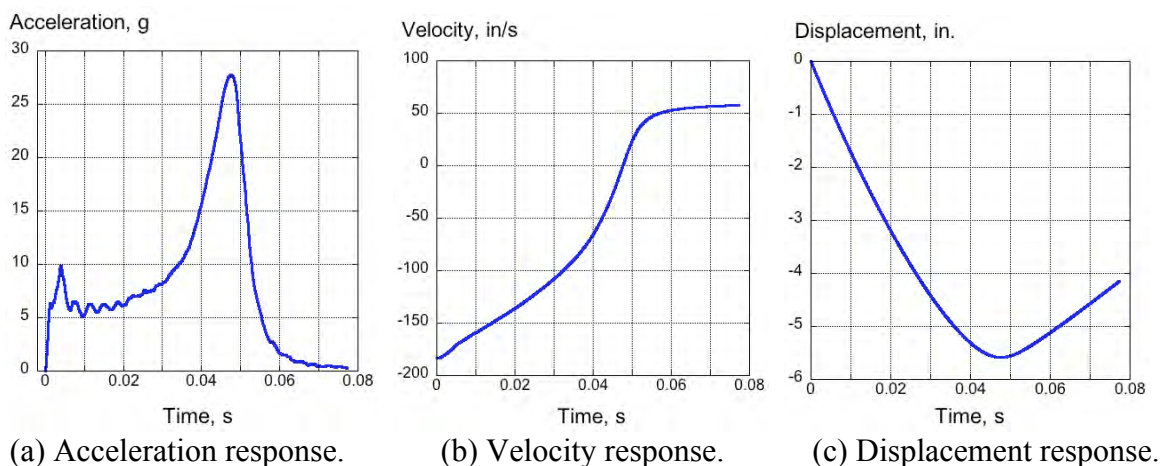(a) Acceleration response.   (b) Velocity response.   (c) Displacement response.

Figure 6. Results of the dynamic crush test of the 68-cell DEA component.

Comparative Analysis of the DEA Component Results
The configuration of the DEA was designed to yield an average crush stress of approximately 20-psi [3]. The dynamic stress-strain responses of the 50-, 104-, and 68-cell DEA components were calculated, as follows. First the raw acceleration data, shown in Figures 3(a), 5(a), and 6(a), were filtered using an SAE CFC 60 low-pass filter [16]. The stress was determined by

multiplying the filtered acceleration data in g's by the weight of the impact block, and then dividing by the cross-sectional area of the DEA. The strain was calculated by double integration of the raw acceleration response to obtain displacement, which was then divided by the initial height of the DEA component. A plot of stress versus strain response for each DEA component is shown in Figure 8. The average stress for each DEA was determined by calculating the area under the stress curve for the strain interval of 0- to 0.4-in/in, and then dividing by 0.4 in/in. The average stress values are 16.5-psi for the 50-cell DEA, 20.8-psi for the 104-cell DEA, and 13.1-psi for the 68-cell DEA.

(a) EA prior to impact.

(b) EA after approximately 35% of crush.

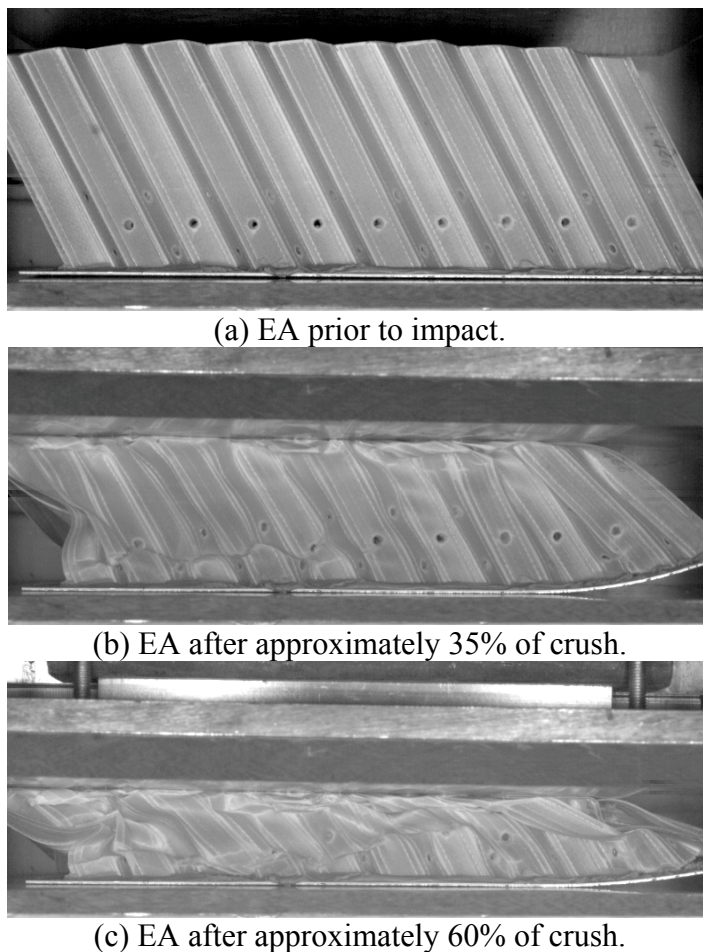(c) EA after approximately 60% of crush.

Figure 7. High-speed video frames from 27° off-axis test.

The reduction in average stress for the 50-cell DEA is attributed to a boundary condition with a larger percentage of unsupported circumferential cells, which tend to fail instead of crushing uniformly, which lowers the effective crush stress. The 104-cell DEA has sufficient cross-sectional area such that these boundary effects are minimized. As mentioned previously, the 68-cell DEA exhibited crushing, as well as bucking of some cells on the perimeter of the component. The large reduction in acceleration following the initial peak, shown in Figure 6(a), is attributed to global buckling of these cells. However, the stiffness of the component is restored as the interior cells crush uniformly and eventually compact. The performance of the DEA concept under off-axis loading is considered good, with only a slight reduction in average acceleration when compared with the 50-cell DEA.
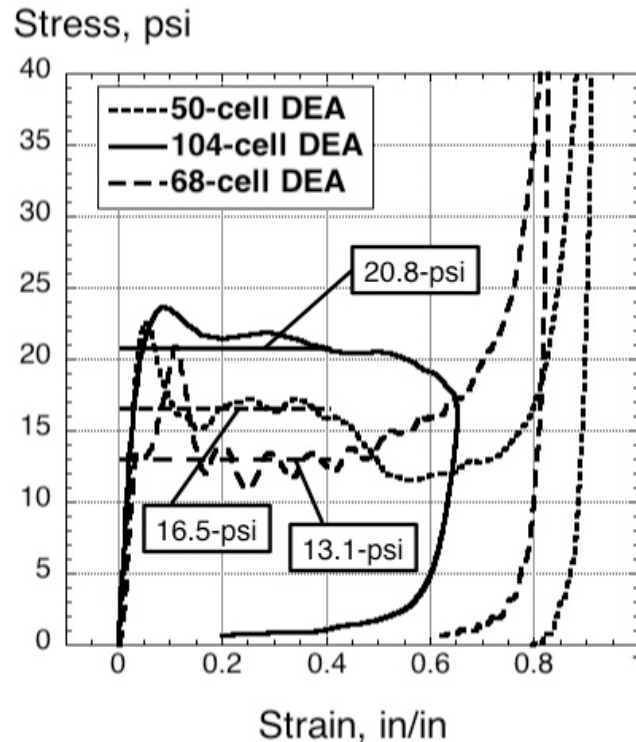
Figure 8. Crush stress versus strain of three DEA components.

LS-DYNA® Solid Element Model Description

Solid-element-based finite element models of the 50-, 104-, and 68-cell DEA components were developed for execution in LS-DYNA® version 971 R4.2. Initially, solid elements were selected for the simulations as a means of lowering execution times, compared with shell-element-based simulations [10, 14-15, 17]. However, it was understood that the use of solid-element-based models precluded the accurate prediction of deformation modes observed in the actual specimens, which would require detailed shell-element-based models [10, 17]. The major challenges of this simulation study were to define a material model that would enable accurate prediction of the dynamic crushing response of the normal (cells are aligned with the loading direction) and off-axis (cells are canted with respect to the loading direction) DEA components; and, to predict both the uniform crush and compaction responses of the DEA components.

The 50-, 104-, and 68-cell DEA models are shown in Figure 9. Each model consists of three parts: the DEA, which is represented using hexagonal solid elements with a nominal element edge length of 0.5-in.; a rigid block constructed of solid hexagonal elements that are assigned a *MAT_RIGID material property; and, an impact surface consisting of quadrilateral shell elements that are assigned the same *MAT_RIGID material property. The edge nodes of the impact surface are fully constrained. The density of the rigid material was chosen such that the weight of each rigid block matched the test conditions shown in Table 1. Likewise, nodal velocities were assigned to the block to match the test conditions. For all models, a contact definition of *CONTACT_AUTOMATIC_SINGLE_SURFACE was used with a coefficient of friction of 0.5. The SOFT parameter in the contact definition was set to 2. The specific details of each DEA component model are given in Table 2.
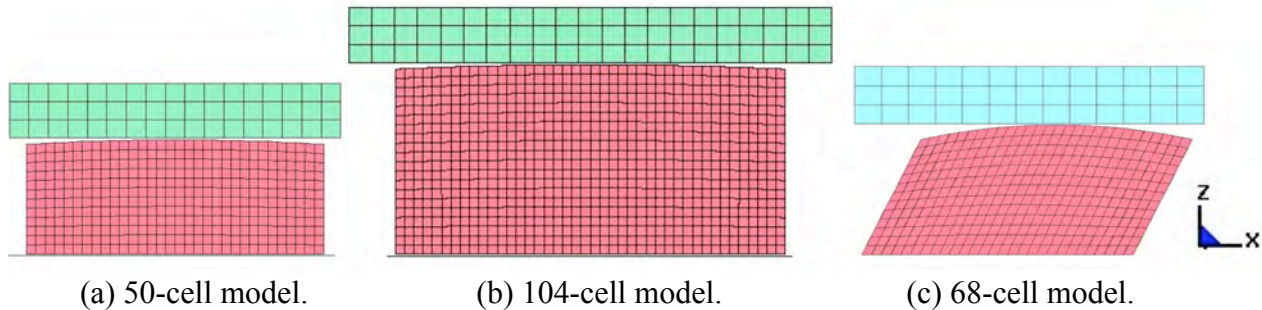
| (a) 50-cell model. | (b) 104-cell model. | (c) 68-cell model. |

Figure 9. Solid-element models of three DEA components.

Table 2. Details of the Solid-Element Models of the DEA Components

Property	50-Cell	104-Cell	68-Cell
Number of nodes	13,123	32,311	14,510
Number of shell elements	225	175	187
Number of solid elements	10,263	28,203	12,233
Nominal solid element edge length	0.5	0.5	0.5
Number of parts	3	3	3

Material Model Development

The material property definitions in LS-DYNA® that were selected to represent the DEA were *MAT_CRUSHABLE_FOAM (Material Type 63), *MAT_HONEYCOMB (Material Type 26), and *MAT_MODIFIED_HONEYCOMB (Material Type 126) [9]. The development of each material model is described in the following subsections.

*MAT_CRUSHABLE_FOAM (Material Type 63)

This material model is intended to represent the properties of isotropic crushable foam and includes optional damping and a tensile cutoff stress. Unloading is fully elastic to the tension cutoff and reloading follows the loading curve. Tension is represented using an elastic-perfectly-plastic response at the tension cutoff value [9]. Mat 63 allows input of a user-defined curve representing the yield stress versus volumetric strain. It is important to note that volumetric strain is defined as 1 minus the relative volume, which is the ratio of the current volume to the initial volume. Thus, as crushing initiates, the volumetric strain is low and increases as crushing progresses.

Input curves representing the stress versus volumetric strain responses of the 50- and 104-cell DEA were developed based on the stress-strain responses shown in Figure 8, which were derived from the filtered acceleration data. Note that the strain calculation represents the change in height of the DEA specimen, which is only one component of the volumetric strain. However, given a low value of Poisson's Ratio (PR=0.05), this approach provides a reasonable approximation of the volumetric strain.

The raw stress-strain data for the 50- and 104-cell DEA components are plotted in Figures 10(a) and (b), respectively, along with the corresponding Mat 63 input curves. Since the 104-cell DEA did not reach the compaction phase during the test, the Mat 63 curve was modified to have the same response as the 50-cell DEA after a strain of 0.8-in/in. For this simulation study, the two Mat 63 curves based on the 50- and 104-cell DEA test data were input as user-defined load

curves in the DEA models. Finally, it should be noted that the unloading curve for this material definition is elastic; however, the experimental responses of the 50- and 104-cell DEA components, shown in Figure 10, indicate that the actual unloading curves are hysteretic.
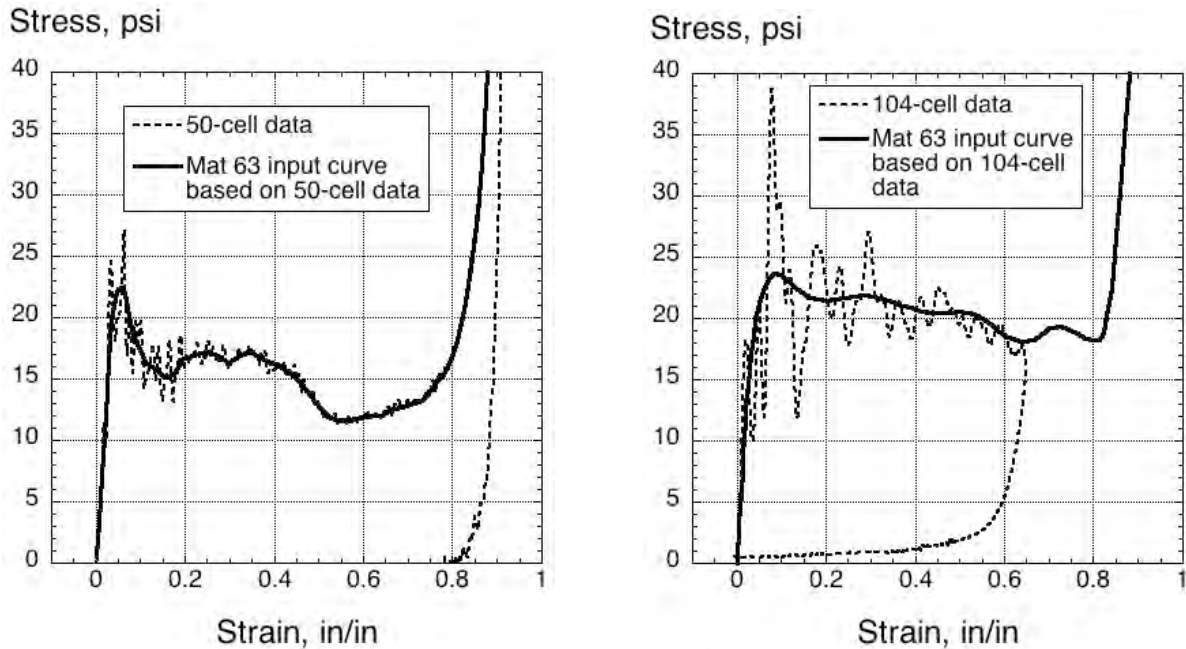
(a) Mat 63 input curve for 50-cell DEA.   (b) Mat 63 input curve for 104-cell DEA.

Figure 10. Mat 63 input load curves and 50- and 104-cell DEA stress-strain responses from tests.

*MAT_HONEYCOMB (Material Type 26)

The Mat 26 material model is used to represent honeycomb and foam materials with anisotropic behavior [9]. Nonlinear elastoplastic material responses are defined separately for normal and shear stresses and these input curves are considered to be fully uncoupled.   The behavior of the material before compaction is orthotropic, where the components in the stress tensor are uncoupled. Unloading is based on the interpolated Young's moduli, which must provide an unloading tangent that exceeds the loading tangent. In this study, the input stress-strain curves are based on volumetric strain and the first value of the curve is less than zero, corresponding to tension, and then increases to full compaction. The user of this material model is cautioned in Reference 9 to ensure that each input curve contains the exact same number of points. This recommendation was followed. The input load curves for Mat 26 were, once again, based on the stress-strain responses of the 50- and 104-cell DEA components, as shown in Figures 11(a) and (b), respectively. Each Mat 26 input curve begins with a point having negative strain and positive stress and the second point has a corresponding value of positive strain and the same value of positive stress, as recommended in Reference 9.

The Mat 26 input curves, shown in Figure 11, correspond to the load curve for sigma-cc (LCC 25401 listed in Table 3) versus volumetric strain [9], where cc represents the local vertical direction. Since no experimental data were available, load curve inputs for the two primary transverse directions (aa and bb) and for the shear directions (s, ab, bc, ca) were based on engineering judgment. The load curves in these directions were assumed to be scaled versions of sigma-cc (LCC 25401), as indicated in Table 3. Finally, Mat 26 allows the user to define directions for the local material axis system using the AOPT parameter [9].   For these

simulations, AOPT was set to 2.0 indicating globally orthotropic behavior with material axes determined by vectors **a** and **d**, such that **a** X **d** defines the primary material direction. For the 50- and 104-cell DEA components, the vectors were chosen such that the primary material direction is oriented vertically. For the 68-cell DEA, the vectors were defined such that the primary material axis for LCC was canted 27° with respect to the vertical direction.
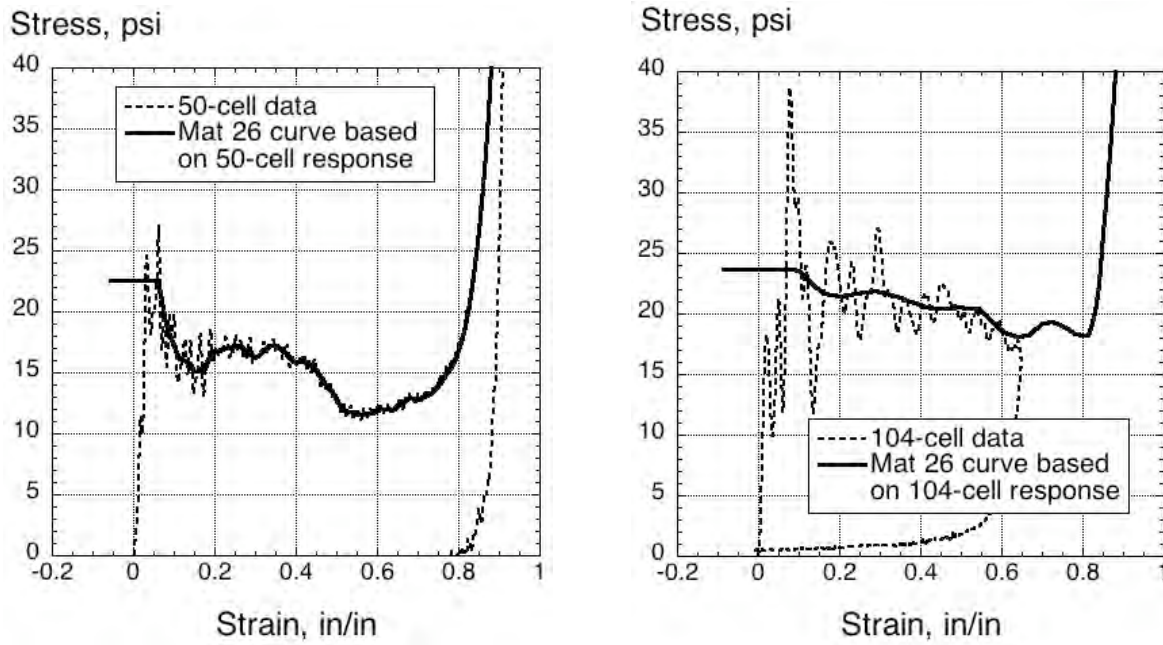
(a) Mat 26 input curve for 50-cell DEA.   (b) Mat 26 input curve for 104-cell DEA.

Figure 11. Mat 26 input curves for the 50- and 104-cell DEA components.

*MAT_MODIFIED_HONEYCOMB (Material Type 126)

Mat 126 was developed to represent the anisotropic material properties of aluminum honeycomb crushable foams and allows three different yield surfaces to be defined, as described in Reference 9. The input for Mat 126 is identical to Mat 26; however, three additional parameters are available that are optional. For the simulations presented in this paper, these parameters were not used. As with Mat 26, all input load curves are recommended to have exactly the same number of points. For Mat 126, the default solid element formulation is type 0, which represents the solid element as a nonlinear spring type brick element. Type 2 hourglass control is recommended. In addition, a second solid element formulation, designated type 9, was developed specifically for Mat 126. Type 9 is a single integration point co-rotational formulation. Element formulations 0 and 9, which are applicable only to Mat 126, were implemented in the code to account for severe element distortions. In formulation 0, the local coordinate system follows the element rotation; whereas in formulation 9, the local coordinate system is based on axes passing through the centroids of the element faces. Formulation 0 is preferred for severe shear deformation when the barrier is fixed in space, whereas formulation 9 is recommended if the barrier is moving and can rotate. Reference 18 describes a simulation study in which Mat 126 was used successfully with the co-rotational element formulation to simulate the orthotropic response of Nomex™ honeycomb. Solid element formulations 0, 1 (constant stress default), and 9 were evaluated in this study. In addition, hourglass control types 1 (standard) and 2 (Flanagan-Belytschko viscous formulation) were evaluated.

Table 3. Transverse and shear load curve scale factors.

LCID	Description	Number	Scale Factor (SF) SF x 25401
LCA	Load curve ID for sigma-aa versus volumetric strain	25400	0.1
LCB	Load curve ID for sigma-bb versus volumetric strain	25400	0.1
LCC	Load curve ID for sigma-cc versus volumetric strain	25401	1.0
LCS	Load curve ID for shear stress versus volumetric strain	25403	0.2125
LCAB	Load curve ID for sigma-ab versus volumetric strain	25402	0.475
LCBC	Load curve ID for sigma-bc versus volumetric strain	25403	0.2125
LCCA	Load curve ID for sigma-ca versus volumetric strain	25403	0.2125

Test-Analysis Correlation Results

Comparisons of predicted and experimental acceleration responses are presented for each DEA component. Three different material models, Mat 63, Mat 26, and Mat 126 were evaluated. For each material model, input curves based on the 50- and 104-cell DEA stress-strain responses were considered. Both sets of input curves were evaluated to account for differences observed in the experimental responses and to determine which input curves best predicted the actual response. Naturally, one would expect the 50-cell DEA response to be best predicted using a material model in which the 50-cell DEA stress-strain input curves are used. However, for completeness, both sets of input curves were evaluated. Correlations with structural deformations are not included since the solid element models cannot accurately replicate the detailed deformation response of the DEA components.

50-Cell DEA Test-Analysis Correlation
The 50-cell DEA component model, shown in Figure 9(a), was executed with three different material models: Mat 63, Mat 26, and Mat 126. Results are shown in Figure 12 in which Mat 63 was used with input curves based on the 50- and 104-cell stress-strain responses. When Mat 63 is used with the 50-cell stress-strain curve, the predicted response matches the initial uniform crushing response of the DEA component, and indicates an increase of acceleration near the end of the pulse, representing compaction of the DEA, as shown in Figure 12(a). However, the magnitude of the compaction response is significantly under predicted. In contrast, the Mat 63 model with the 104-cell stress-strain input curve over predicts the uniform crushing response and no compaction phase is predicted, as shown in Figure 12(b).

Test-analysis correlation results are shown in Figures 13(a) and (b) in which the 50-cell DEA model was executed with Mat 26 using the 50- and 104-cell DEA input stress-strain responses, respectively. The Mat 26 material model with the 50-cell input curve does a much better job of predicting the magnitude of the compaction response, as shown in Figure 13(a). In comparison, when Mat 63 is used with the 50-cell stress-strain input curve, the predicted response indicates only a slight increase of acceleration near the end of the pulse, as shown in Figure 12(a). Predictions from the Mat 26 model with the 104-cell DEA input response, shown in Figure 13(b), indicate a higher uniform crushing response than seen in the experimental response and no compaction is predicted.
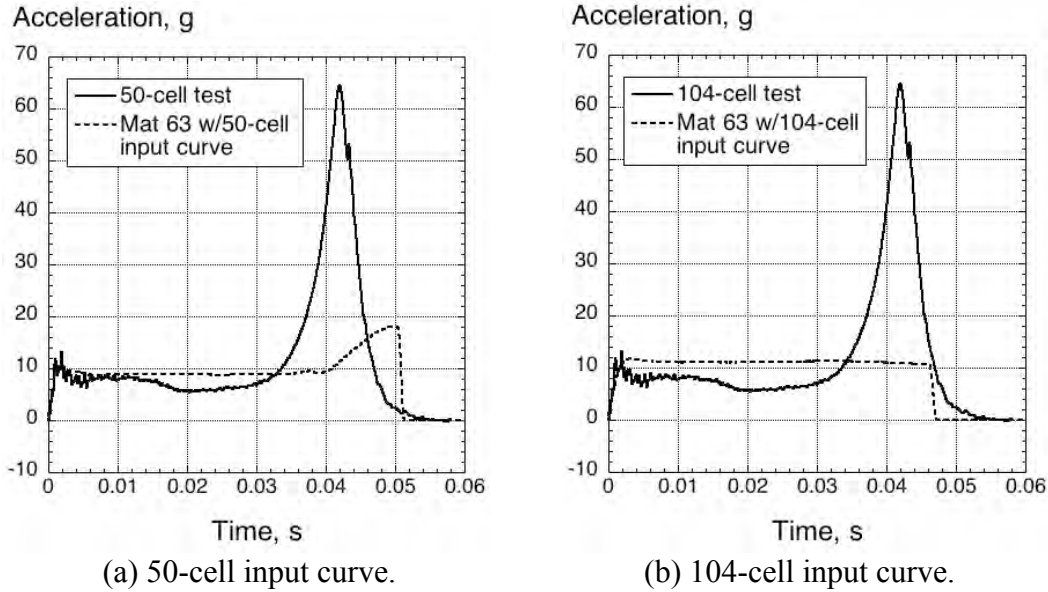
(a) 50-cell input curve.   (b) 104-cell input curve.

Figure 12. Test-analysis correlation of the 50-cell DEA with **Mat 63** material models.

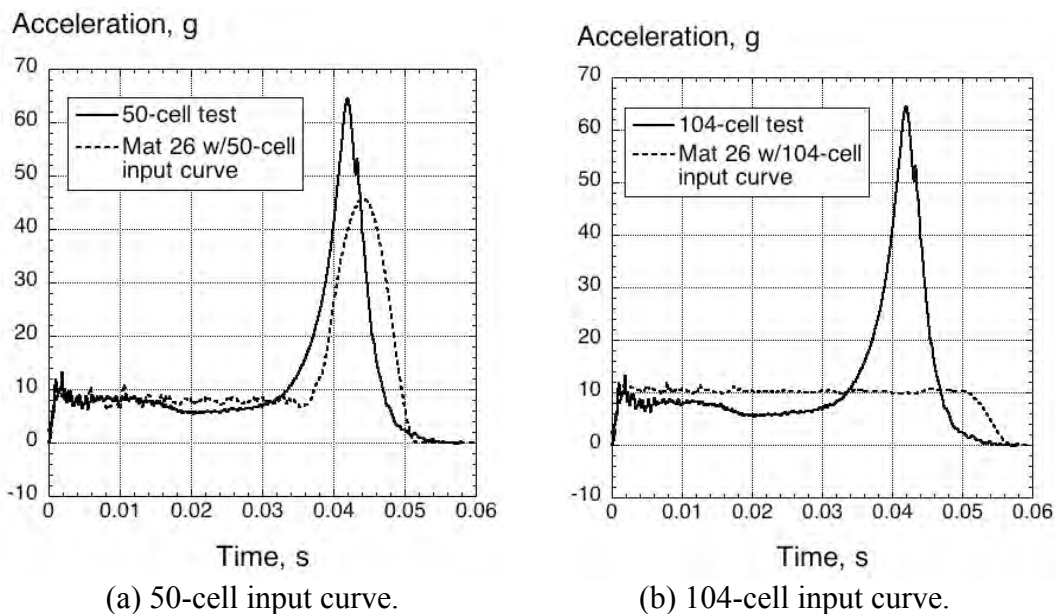(a) 50-cell input curve.   (b) 104-cell input curve.

Figure 13. Test-analysis correlation of the 50-cell DEA with **Mat 26** material models.

When the 50-cell DEA model was executed using Mat 126, problems were observed with contact penetration, severe element distortion, and high values of hourglass energy in comparison with the total energy of the simulation. Modifications were made to the model in an attempt to resolve these problems including: (1) refining the meshes of the impact surface and the rigid block, (2) changing the rigid material properties of the block and the impact surface to elastic with a low value of Young's Modulus, (3) fixing all of the nodes in the impact surface rather than just the edge nodes, (4) increasing the thickness of the impact surface, and (5) modifying the SOFT parameter in the contact definition. The modified model was executed with two different Hourglass (HG) types 1 (standard) and 2 (viscous formulation), and three different solid Element Formulations (EF) of 0, 1, and 9. However, none of these modifications were successful in remedying the contact and hourglass issues with these simulations.

104-Cell DEA Test-Analysis Correlation
The 104-cell DEA component model, shown in Figure 9(b), was also executed with three different material models: Mat 63, Mat 26, and Mat 126. Test-analysis correlation results are shown in Figure 14(a) and (b) in which Mat 63 was used with the 50- and 104-cell stress-strain input responses, respectively. Of the material models considered, the Mat 63 material model with the input curve based on the 50-cell data provides the best correlation with experiment, in general. This finding is surprising in that one would expect that the Mat 63 model with the 104-cell input to provide the best correlation. The predicted response plotted in Figure 14(a) simulates the initial peak acceleration and a lower uniform crushing stress of the DEA than seen in Figure 14(b). Also, the predicted response, shown in Figure 14(a), exhibits a gradual reduction in acceleration, as seen in the experimental response, until the acceleration falls off sharply at 0.056-s.

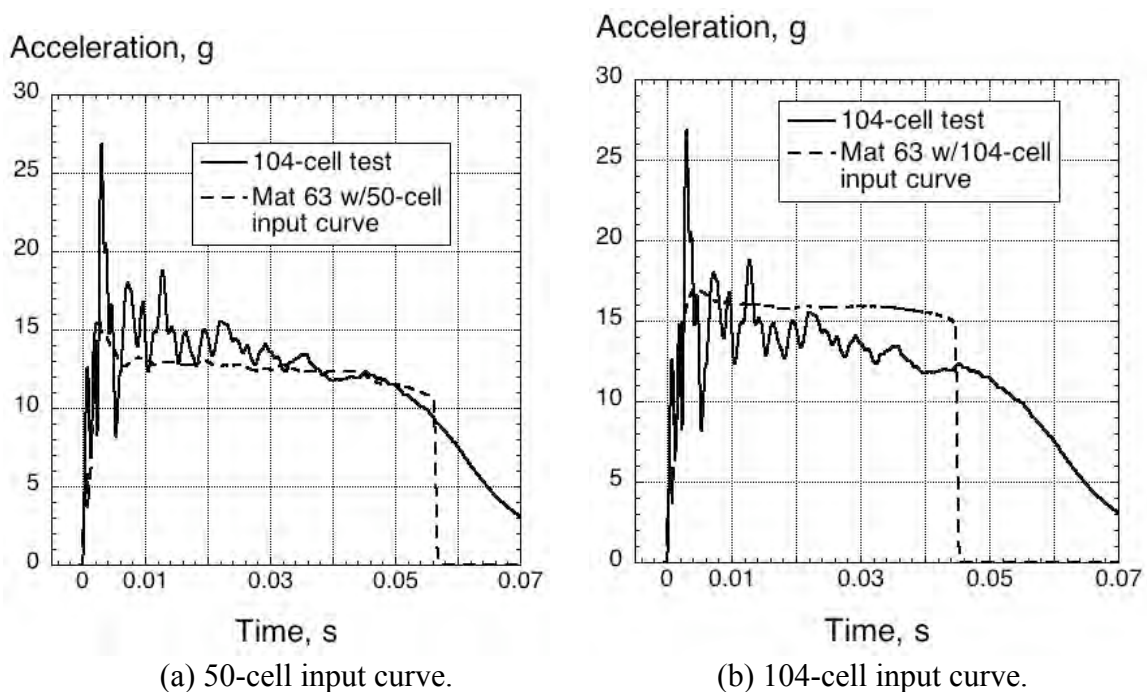(a) 50-cell input curve.   (b) 104-cell input curve.

Figure 14. Test-analysis correlation of the 104-cell DEA with **Mat 63** material models.

Results for Mat 26 are shown in Figure 15, in which the two input curves, shown in Figure 11, were considered. In this case, the Mat 26 material model with 104-cell input curves shows the best correlation with experiment, as expected. This model matches the uniform crushing response of the 104-cell DEA component exactly to approximately 0.03-s, after which time the experimental response begins to gradually decrease.

When the 104-cell DEA model was executed with Mat 126, similar problems were observed with contact penetration, element distortion, and high values of hourglass energy, as seen with the 50-cell DEA simulation using Mat 126. The same modifications were made to the model in an attempt to resolve these problems. The resulting modified model was then executed with two different Hourglass (HG) types 1 (standard) and 2 (viscous), and three different solid Element Formulations (EF) of 0, 1, and 9. However, none of these modifications were successful in remedying the contact and hourglass issues with these simulations.

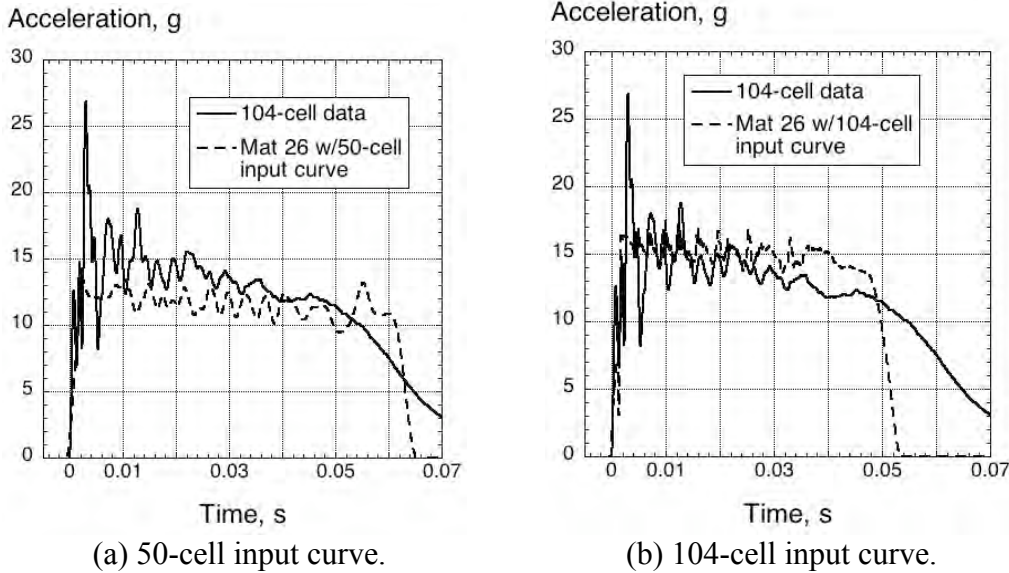(a) 50-cell input curve.   (b) 104-cell input curve.

Figure 15. Test-analysis correlation of the 104-cell DEA with **Mat 26** material models.

68-Cell DEA Test-Analysis Correlation

The 68-cell DEA component model, which is canted at 27° as shown in Figure 9(c), was executed with the same three different material models: Mat 63, Mat 26, and Mat 126. Test-analysis correlation results are shown in Figure 16(a) and (b) in which Mat 63 was used with the 50- and 104-cell stress-strain input responses, respectively. Mat 63 is intended for isotropic materials and does not offer a mechanism to account for the off-axis orientation of the DEA. As a result, neither model does a good job of predicting the experimental response. One possible resolution in this case would be to multiple the input curves by the cosine of the cant angle (27°), to account for the off-axis orientation of the cells; however, this approach was not attempted.

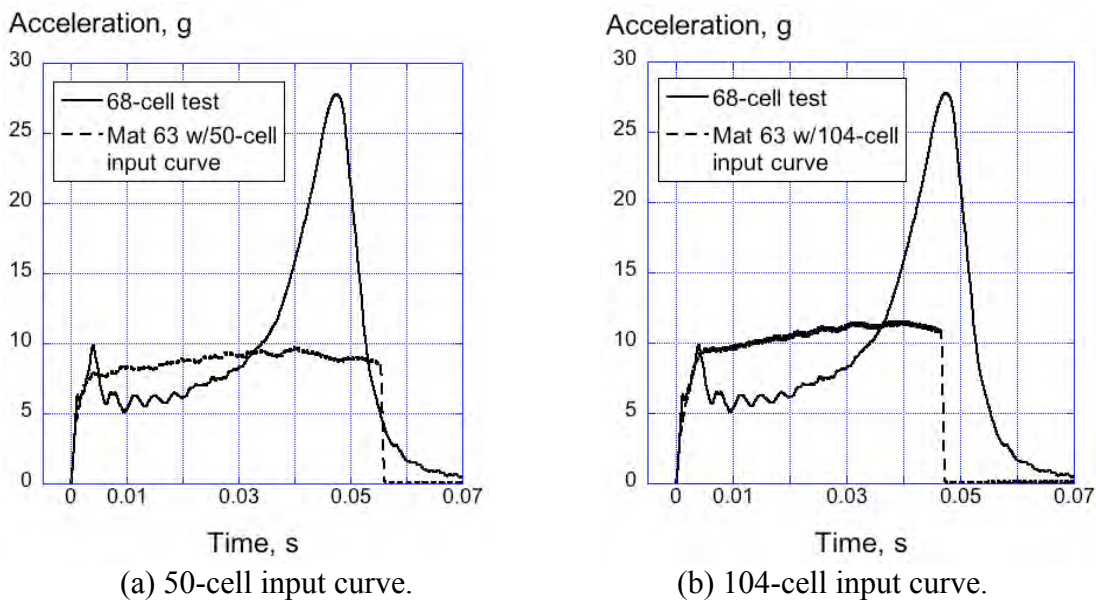(a) 50-cell input curve.   (b) 104-cell input curve.

Figure 16. Test-analysis correlation of the 68-cell DEA with **Mat 63** material models.

Test-analysis comparisons for Mat 26 are shown in Figure 17, in which the two curves of Figure 11 were used as input to the material model. Note that Mat 26 allows the local material directions to be input using the AOPT parameter. The results shown in Figure 17(a) indicate that the Mat 26 material model with 50-cell DEA stress-strain input curves demonstrates the best agreement with test data. However, the analysis over predicts the peak acceleration of the compaction response of the 68-cell DEA and the timing of the peak is not well predicted. Finally, the simulation results for the Mat 26 material model with 104-cell DEA input curves over predicts the crushing response of the 68-cell DEA and no compaction behavior is predicted.

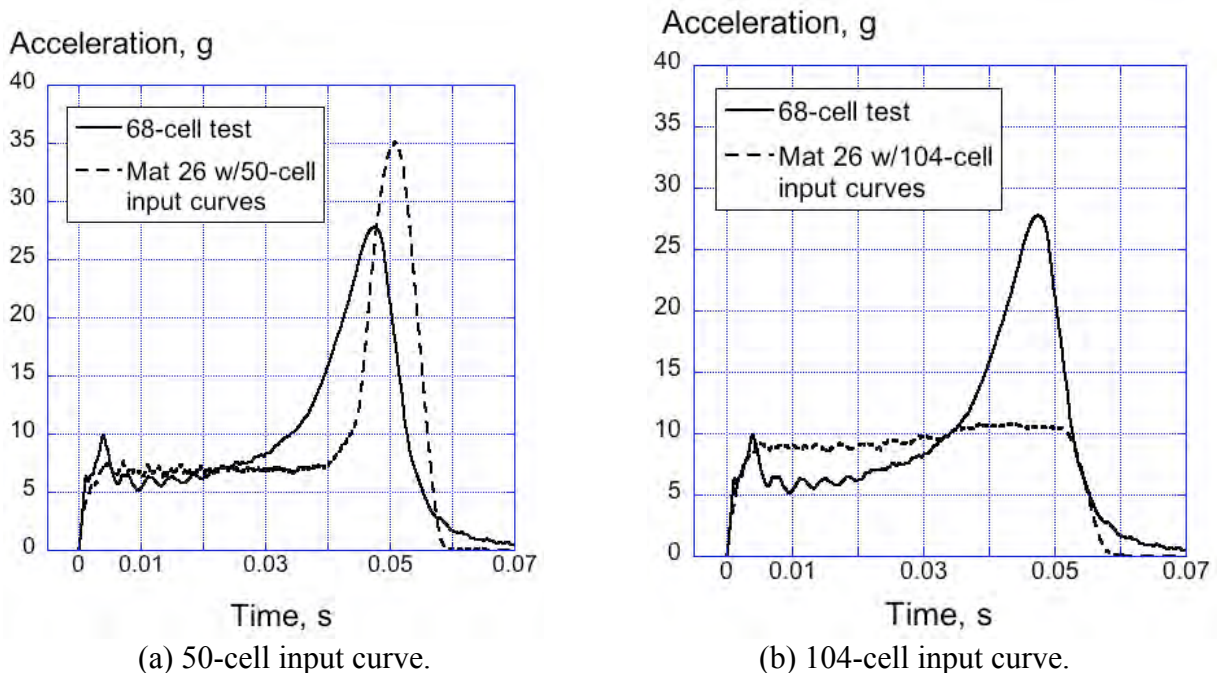(a) 50-cell input curve.   (b) 104-cell input curve.

Figure 17. Test-analysis correlation of the 68-cell DEA with **Mat 26** material models.

Unlike the 50- and 104-cell models, the 68-cell canted model executed with Mat 126 material properties without contact or hourglass issues. Consequently, no modifications were made to the original 68-cell model. For these simulations, the 50- and 104-cell stress-strain input curves, shown in Figure 11, were evaluated. Two different Hourglass (HG) types, 1 (standard) and 2 (viscous), and three different solid Element Formulations (EF), 0, 1, and 9, were evaluated. These parameters were examined because hourglass control type 2 and element formulations 0 and 9 are specifically recommended for Mat 126 [9]. The results of the simulations with the Mat 126 material model based on the 50-cell input curves are shown in Figure 18. Two plots are included: one with HG equal 1 and varying EF, as shown in Figure 18(a); and, the second with HG equal 2 and varying EF, as shown in Figure 18(b). The simulations with EF=9 failed prematurely due to severe element distortion; consequently, no results are shown in Figure 18 for this case.

The results shown in Figure 18 indicate that no differences are observed due to changes in element formulation for a given value of hourglass control type, i.e. the EF=0 and EF=1 curves are virtually identical for HG=1 and HG=2. Also, the four simulation curves in Figure 18 over predict the crush response slightly and under predict the peak of the compaction response.

                    (a) HG=1, EF=0 and 1.   (b) HG=2, EF=0 and 1.
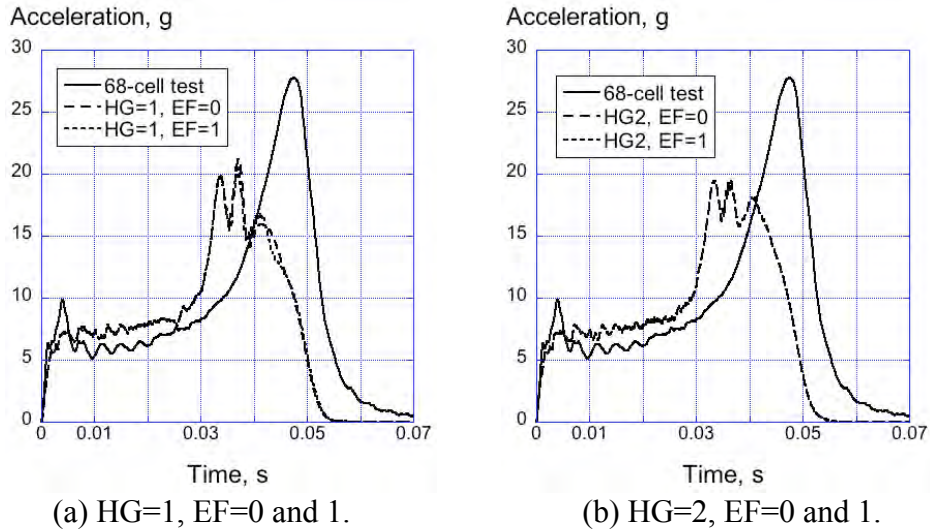
Figure 18. Correlation of the 68-cell DEA with **Mat 126**, based on the 50-cell input load curves.

The results for the simulations using the Mat 126 material model with the 104-cell input curves are shown in Figure 19. Two plots are included: one with HG equal 1 and varying EF equal 0, 1, 9, as shown in Figure 19(a); and, the second with HG equal 2 and varying EF equal 0, 1, and 9, as shown in Figure 19(b). In both simulations where EF=9 was used, the model performed well initially and then failed before reaching the termination time of the simulation. Also, regardless of the type of hourglass control used, the simulations using EF=0 did not predict the compaction phase of the 68-cell DEA test response. The best correlation was demonstrated with EF=1, which is the default constant stress solid element formulation. The EF=1 simulations under predicted the peak acceleration of the compaction phase and missed the timing of the peak. However, these results represent the first time that a material model with the 104-cell stress-strain curves as input was used to predict both the crushing and compaction responses of the DEA.
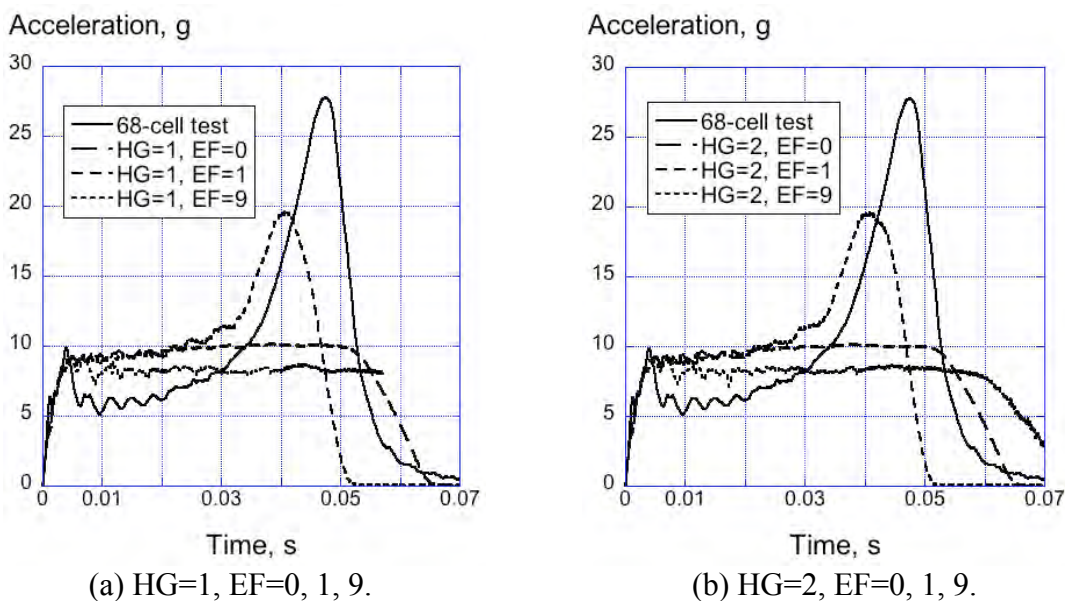

                    (a) HG=1, EF=0, 1, 9.   (b) HG=2, EF=0, 1, 9.

Figure 19. Correlation of the 68-cell DEA with **Mat 126**, based on the 104-cell input curves.

Discussion of Results

Several factors played a role in this test-analysis correlation study. First, dynamic crush responses were obtained from testing three individual DEA components. No repeated tests were conducted, which would have provided some indication of the scatter in the test data. Secondly, the DEA was designed to achieve a 20-psi average crush stress. However, based on the data shown in Figure 8, the average crush stress for the two normal components ranged from 13.1- to 20.8-psi. The reduction in average stress for the 50-cell DEA is attributed to a larger percentage of circumferential cells, which tend to fail catastrophically instead of crushing uniformly, which lowers the effective crush stress. However, it is interesting to note that the simulations that were performed using the 50-cell input load curves, generally did a better job of predicting the compaction response that did the simulations performed using the 104-cell input load curves, see Figures 12-13 and 17. Finally, no tests were conducted to determine transverse or shear responses of the DEA. Consequently, the input load curves for these directions were based on engineering judgment, as indicated in Table 3.

As mentioned previously, the simulations of the 50- and 104-cell DEA components that were executed using Mat 126 had problems with contact penetration, severe element distortion, and excessive hourglass energy. According to References 19 and 20, Mat 126 can generate gross errors and provide non-physical deformations when used to predict the response of anisotropic foam materials. The information provided in Reference 19 implies that Material Type 142 (*MAT_TRANSVERSELY_ANISOTRIPC _CRUSHABLE_FOAM) may be a better choice for simulating the DEA response. Future DEA simulations will be conducted to evaluate this material model.

The LS-DYNA® manuals [8, 9] recommend that the viscous hourglass formulation (type 2) be used with Mat 126. Further recommendations were that solid element formulation type 0 and type 9 be used, depending on whether or not a moving barrier was used in the model. For the Mat 126 simulations performed for the 68-cell DEA, hourglass types 1 and 2 and solid element formulations 0, 1, and 9 were investigated. The models that were executed with element formulation type 9 developed problems and did not execute to termination, though data was presented where valid responses were obtained. For Mat 126 with 104-cell input curves, the model with element formulation type 0 did not predict the compaction response of the 68-cell DEA, as shown in Figure 19. For this case, only element formulation type 1 was successful in predicting both the uniform crushing and the compaction response. These findings are counter to the recommendations made in the LS-DYNA® manuals [8, 9].

Conclusions

Three different material models were evaluated in LS-DYNA® to determine if they could be used in conjunction with solid-element-based models of a composite honeycomb energy absorber to predict both the uniform crushing and compaction responses under normal and off-axis loading. The three material models were Mat 63 (crushable foam), Mat 26 (honeycomb), and Mat 126 (modified honeycomb). Three multi-cell DEA components were manufactured using a hexagonal cell geometry in which the cell wall edge length was 1.0-in. and the nominal cell wall thickness was 0.01-in. Each of these components was fabricated from a single layer of Kevlar™-129 fabric/epoxy oriented at ±45° with respect to the longitudinal cell axis. Two of the DEA

components, consisting of 50 and 104 cells, were manufactured such that the longitudinal axes of the cells were oriented vertically, or in the same direction as loading. A third DEA component, consisting of 68 cells, was fabricated such that the longitudinal axes of the cells were canted by 27° with respect to the loading direction.

The simulation results indicate that, with the proper input curve, Mat 63 can be used to predict the uniform crushing and, to a lesser degree, the compaction response of the DEA under normal loading conditions. However, Mat 63 has no mechanism to account for changes in the local material axis system, since this material model is intended for isotropic materials only. Consequently, this material model was not capable of predicting the compaction response of the 68-cell canted DEA. In contrast, Mat 26 was used to predict both the uniform crushing and compaction responses of the 50-, 104- and 68-cell DEA components with reasonable success. The degree of correlation was highly dependent on the choice of input curve.

Finally, issues related to contact penetration, severe element distortion, and excessive hourglass energy were found with the 50- and 104-cell simulations using Mat 126. Several modifications to the model were implemented in an attempt to resolve these issues; however, the problems persisted. In contrast, Mat 126 was used successfully in simulating the 68-cell canted DEA response, without changes to the model. For these simulations, two different hourglass control types, 1 (standard) and 2 (viscous), were evaluated, as well as three different solid element formulations: 0, 1, and 9. These parameters were examined because hourglass control type 2 and element formulations 0 and 9 are specifically recommended for Mat 126. However, models in which element formulation type 1 was specified demonstrated the best correlation. The 68-cell DEA models using Mat 126 with element formulation type 1 were able to predict both the uniform crushing and compaction phases of the response, regardless of which hourglass control type was specified.

References

1. Jackson, K.E., Fuchs, Y. T., and Kellas, S., "Overview of the NASA Subsonic Rotary Wing Aeronautics Research Program in Rotorcraft Crashworthiness," *Journal of Aerospace Engineering*, Special Issue on Ballistic Impact and Crashworthiness of Aerospace Structures, Volume 22, No. 3, July 2009, pp. 229-239.

2. Kellas, S., "Deployable Rigid System for Crash Energy Management," US Patent Nos. 6,755,453 on June 29, 2004; 6,976,729 on December 20, 2005; and 7,040,658 on May 9, 2006.

3. Kellas, S. and Jackson, K. E., "Deployable System for Crash-Load Attenuation," Proceedings of the 63ʳᵈ American Helicopter Society (AHS) Forum, VA Beach, VA, May 1-3, 2007.

4. Kellas, S. and Jackson, K. E., "Multi-Terrain Vertical Drop Tests of a Composite Fuselage Section," Proceedings of the 64ᵗʰ American Helicopter Society (AHS) Annual Forum, Montreal, Canada, April 29-May 1, 2008.

5. Yosef V., BenMoshe A, Noyman Y., Gansman B., and Bradney C., "Rotorcraft External Airbag Protection System," Proceedings of the American Helicopter Society 62ⁿᵈ Annual Forum, Phoenix AZ, May 9-11, 2006.

6. Bolukbasi, A., "Active Crash Protection Systems for UAVs," Proceedings of the American Helicopter Society (AHS) 63ʳᵈ Annual Forum, Virginia Beach, VA, May 1-3, 2007.

7. Kellas, S., Jackson, K. E., and Littell, J. D., "Full Scale Crash Test of a MD-500 Helicopter with Deployable Energy Absorbers," Proceedings of the 66ᵗʰ AHS Forum, Phoenix, AZ, May 11-13, 2010.

8. Hallquist, John O., "LS-DYNA® Keyword User's Manual Volume I," Version 971, Livermore Software Technology Corporation, May 2007.

9. Hallquist, John O., "LS-DYNA® Keyword User's Manual Volume II Material Models," Version 971, Livermore Software Technology Corporation, May 2007.

10. Polanco, M., Kellas, S., and Jackson, K. E., "Evaluation of Material Models within LS-DYNA for a Kevlar/Epoxy Composite Honeycomb," Proceedings of the 65th AHS Forum, Grapevine, TX, May 27-29, 2009.

11. Horta, L. G., Jackson, K. E., and Kellas, S., "A Computational Approach for Model Update of an LS-DYNA Energy Absorbing Cell," Proceedings of the 64th American Helicopter Society (AHS) Annual Forum, Montreal, Canada, April 29-May 1, 2008.

12. Jackson, K. E., and Fuchs, Y. T., "Comparison of ALE and SPH Simulations of Vertical Drop Tests of a Composite Fuselage Section into Water," Proceedings of the 10th International LS-DYNA Users Conference, Dearborn, MI, June 8-10, 2008.

13. Fasanella, E. L., Jackson, K. E., and Kellas, S., "Soft Soil Impact Testing and Simulation of Aerospace Structures," Proceedings of the 10th LS-DYNA Users Conference, Dearborn, MI, June 8-10, 2008.

14. Annett, Martin S., "LS-DYNA Analysis of a Full-Scale Helicopter Crash Test," Proceedings of the 11th LS-DYNA Users Conference, Dearborn, MI, June 6-8, 2010.

15. Annett, M. S., and Polanco, M. A., "System-Integrated Finite Element Analysis of a Full-Scale Helicopter Crash Test with Deployable Energy Absorbers," Proceedings of the 66th AHS Forum, Phoenix, AZ, May 11-13, 2010.

16. Society of Automotive Engineers, Recommended Practice: Instrumentation for Impact Test - Part 1, Electronic Instrumentation, SAE J211/1, March 1995.

17. Polanco, M. A., "Use of LS-DYNA to Assess Impact Response of a Shell-Based Kevlar/Epoxy Composite Honeycomb," Proceedings of the 11th International LS-DYNA Users Conference, Dearborn, MI, June 6-8, 2010.

18. Heimbs, S., Middendorf, P., and Maier, M., "Honeycomb Sandwich Material Modeling for Dynamic Simulations of Aircraft Interior Components," Proceedings of the 9th International LS-DYNA Users Conference, Dearborn, MI, June 4-6, 2006.

19. Hirth, A., Du Bois, P., and Weimar, K., "A Material Model for Transversely Anisotropic Crushable Foams in LS-DYNA," Proceedings of the 7th International LS-DYNA Users Conference, Detroit, MI, 2002.

20. Hassen, A. G., Langseth, M., and Hopperstad, O. S., "Crash Behavior of Foam-based Components: Validation of Numerical Simulations," *Advanced Engineering Materials*, Vol. 4, No. 10, 2002, pp. 771-776.